PNAS RESEARCH ARTICLE | BIOPHYSICS AND COMPUTATIONAL BIOLOGY OPEN ACCESS

Structural basis of human $Na_v1.5$ gating mechanisms

Rupam Biswas[a], Ana Laura López-Serrano[a,b], Apoorva Purohit[c], Angelina Ramirez-Navarro[a,b], Hsiang-Ling Huang[a], Giovanna Grandinetti[a,d], Xiaolin Cheng[c,e], Sarah M. Heissler[a], Isabelle Deschênes[a,b,1], and Krishna Chinthalapudi[a,1]

Affiliations are included on p. 8.

Edited by Robert Stroud, University of California San Francisco, San Francisco, CA; received August 9, 2024; accepted April 14, 2025

Voltage-gated $Na_v1.5$ channels are central to the generation and propagation of cardiac action potentials. Aberrations in their function are associated with a wide spectrum of cardiac diseases including arrhythmias and heart failure. Despite decades of progress in $Na_v1.5$ biology, the lack of structural insights into intracellular regions has hampered our understanding of its gating mechanisms. Here, we present two cryo-EM structures of human $Na_v1.5$ in open states, revealing sequential conformational changes in gating charges of the voltage-sensing domains (VSDs) and several intracellular regions. Despite the channel being in the open state, these structures show repositioning, but no dislodging of the IFM motif in the receptor site. Molecular dynamics analyses show our structures with CTD conduct Na^+ ions. Notably, our structural findings highlight a dynamic C-terminal domain (CTD) and III-IV linker interaction, which regulates the conformation of VSDs and pore opening. Electrophysiological studies confirm that disrupting this interaction alters fast inactivation of $Na_v1.5$. Together, our structure–function studies establish a foundation for understanding the gating mechanisms of $Na_v1.5$ and the mechanisms underlying CTD-related channelopathies.

sodium channels | action potentials | cryo-EM | electrophysiological studies | arrhythmias

Significance

The cardiac voltage-gated sodium channel $Na_v1.5$ is essential for normal heart function and excitability, with dysfunctions linked to various arrhythmias and heart failure. Achieving a comprehensive understanding of the structural mechanisms of $Na_v1.5$ is critical for the mechanistic understanding of cardiac physiology and congenital arrhythmias caused by $Na_v1.5$ mutations and for the development of novel targeted therapeutics. Here, we present cryo-EM structures of the cardiac $Na_v1.5$ α-subunit in the open state. Together with functional studies, we show how the intracellular C-terminal domain interacts with the III-IV linker that allosterically regulates voltage-sensing domains and pore opening of $Na_v1.5$. Our study reveals a previously unidentified fast inactivation mechanism of $Na_v1.5$, offering insights into its functional dynamics.

The cardiac voltage-gated sodium (Na_v) channel $Na_v1.5$ is essential for cardiac excitability and conduction (1). $Na_v1.5$ initiates the rapid influx of extracellular sodium ions into the cytosol during the upstroke of the cardiac action potential. Alterations in Na^+ currents have been implicated in the etiology of arrhythmias (2, 3). Hundreds of mutations in *SCN5A*, the gene encoding for $Na_v1.5$, have been linked to arrhythmia syndromes such as Brugada syndrome (BrS) and long QT syndrome type 3 (LQT3) (4). Hence, understanding the structure and function of $Na_v1.5$ is pivotal for unraveling the molecular basis of cardiac electrical activity and developing targeted therapies for arrhythmias and other related disorders.

Eukaryotic Na_v channels are composed of a pore-forming α subunit and auxiliary β subunits (5). The α subunit consists of four homologous domains (D_I to D_{IV}) that share significant similarities yet exhibit different functions. Each domain is composed of six transmembrane segments referred to as S1 to S6. The voltage-sensing domain (VSD, S1 to S4) and the pore-forming domain (PD, S5 to S6) are arranged in a pseudotetrameric manner (6, 7). The N-terminal domain (NTD) and the C-terminal domain (CTD) are located in the cytosol. During the cardiac action potential, Na_v channels get activated and rapidly transition into a nonconductive state known as the fast inactivated state (8). This transition occurs within 2 to 3 ms following fast activation and is followed by the return of the channel to the resting state upon repolarization (8).

Functional studies identified the Isoleucine-Phenylalanine-Methionine (IFM) motif in the linker between D_{III} and D_{IV} (III-IV linker) as crucial for fast inactivation (9). Published structures of Na_v channels showed that the IFM motif gets sequestered into a receptor binding pocket distant from the pore which leads to the proposed "door wedge" model for fast inactivation (10–14). It was also shown that mutations that hinder the interactions between the IFM motif and its receptor binding pocket allosterically propagate to the S6 segments (11, 15). Another model suggests that residues located at the intracellular end of the pore-forming S6 segment, rather than the IFM motif, cause fast inactivation (16). Published work also implied a role for the CTD in regulating sodium channel function (17–21). Indeed, the replacement of the native CTD of $Na_v1.5$ with that of $Na_v1.4$ confers inactivation kinetics that mimics $Na_v1.4$ and vice versa (18, 19, 22). Additionally, the CTD is a hotspot for LQT3 mutations that affect fast inactivation (23). Although electrophysiological and structural studies have identified critical functional elements, the molecular and structural mechanisms underlying fast inactivation, and especially the role of the CTD have yet to be established in the framework of full-length structures of $Na_v1.5$. Although over the past three decades, there has been significant advancement in the

Author contributions: I.D. and K.C. designed research; R.B., A.L.L.-S., A.P., A.R.-N., H.-L.H., G.G., and S.M.H. performed research; A.R.-N., H.-L.H., G.G., X.C., S.M.H., I.D., and K.C. contributed new reagents/analytic tools; R.B., A.L.L.-S., A.P., and K.C. analyzed data; and R.B., A.L.L.-S., A.P., X.C., S.M.H., I.D., and K.C. wrote the paper.

The authors declare no competing interest.

This article is a PNAS Direct Submission.

[1]To whom correspondence may be addressed. Email: isabelle.deschenes@osumc.edu or krishna.chinthalapudi@osumc.edu.

This article contains supporting information online at https://www.pnas.org/lookup/suppl/doi:10.1073/pnas.2416181122/-/DCSupplemental.

Published May 14, 2025.

understanding of $Na_v1.5$ function, our insights into fast inactivation mechanisms remain limited due to incomplete structural knowledge of the intracellular regions.

Here, we report two distinct high-resolution cryoelectron microscopy (cryo-EM) structures of human full-length $Na_v1.5$ ($hNa_v1.5$) in the open state. The structures feature significant conformational changes in the VSDs and exhibit high plasticity in the positioning of the intracellular CTD and the III-IV linker. Furthermore, sodium ion conductance is observed in our open state structure through molecular dynamics (MD) simulations. The structures show previously unseen intracellular regions of $Na_v1.5$ including the NTD and the CTD. Site-directed mutagenesis coupled with electrophysiological measurements show that the disruption of interactions between the CTD and the III-IV linker results in compromised fast inactivation of $hNa_v1.5$. In summary, our findings elucidate the mechanism for fast inactivation and settle the contribution of the CTD in maintaining the open state.

Results

The Overall Architecture of Full-Length $hNa_v1.5$. We purified recombinant full-length $hNa_v1.5$ from Expi293 cells (*SI Appendix*, Fig. S1*A*). Negative stain electron microscopy and SDS-PAGE demonstrated the purity of our protein preparations (*SI Appendix*, Fig. S1 *B* and *C*). We used optimal screened grids for cryo-EM data collection. Analysis of our cryo-EM data showed significant heterogeneity owing to the flexible intracellular regions of $hNa_v1.5$. We assessed the structural heterogeneity by establishing a data processing workflow where particles were clustered into four classes based on the presence of intracellular features (*SI Appendix*, Fig. S2*A*). Class 1 and class 2 contained the core membrane domain and intracellular regions of $hNa_v1.5$ (*SI Appendix*, Fig. S2*A*). The processed data yielded structures of $hNa_v1.5$ with overall resolutions of ~3.6 Å for Class 1 (Model-I), and ~3.9 Å for Class 2 (Model-II) (*SI Appendix*, Figs. S2*B* and S3 *A*–*C*). Model-I and Model-II comprise a total of ~1,400 residues each and contain the transmembrane core, extracellular regions, the III-IV linker, portions of the I-II and II-III linker, NTD, and the EF-hand domain of the CTD (Fig. 1*A*). The cryo-EM reconstructions show unambiguous densities for the VSDs, the selectivity filter, and the pore-lining S6 segments (*SI Appendix*, Figs. S4–S8). The NTD, CTD, and other intracellular regions exhibit lower local resolutions due to their flexibility (*SI Appendix*, Figs. S2 and S6). The α subunit of $hNa_v1.5$ shows a pseudotetrameric structure consisting of the D_I to D_{IV} domains in a domain-swapped manner (Fig. 1 *A* and *B*), consistent with the overall architecture observed in published structures of Na_v channels (10–13, 24–26). The NTD and the CTD emanate from the transmembrane portion of the channel on the intracellular side. The NTD is located at the base of VSD_I. The CTD is a compact domain that is connected to the S6-helix of the D_{IV} via a flexible linker. Its position is variable with respect to the core transmembrane domain (Fig. 1 *A* and *B*). The RMSD between Model-I and Model-II is 0.7 Å for 1,113 Cα atoms. The transmembrane cores of Models-I and -II have an RMSD of 1.6 Å to 1.8 Å over ~1,100 Cα atoms compared to the human $Na_v1.5$-E1784K structure (PDB ID: 7DTC) and show an overall outward dilation of ~5 to 6 Å (Fig. 2*A* and Movie S1). This structural change is accompanied by the expansion of the pore domain (Fig. 2*A* and Movie S1). In Model-II, the lateral movements of the S6 segments have resulted in the outward displacement of the Cα backbone of the S4–S5 linker helices. Consequently, all the VSDs have translocated laterally across the membrane. The superimposition of each VSD in Model-II with $Na_v1.5$-E1784K (PDB ID: 7DTC) and $rNa_v1.5c$/QQQ (PDB ID: 7FBS), aligned over their S2 segments, revealed distinct extents of tilting, vertical movements of S4 segments which carry the gating charges (Fig. 2*B*). However, the superimposition of S2 and S4 segments of $Na_v1.5$-E1784K and $rNa_v1.5c$/QQQ showed only minor changes (Fig. 2*B* and *SI Appendix*, Fig. S9). The NTD is stabilized by the $S6_I$ segment in our open state structures, which was also resolved in a recent cryo-EM structure of the $rNa_v1.5$/BTX-B (PDB ID: 8T6L) complex (27). However, the structural comparison of Model-II with $rNa_v1.5$/BTX-B revealed a dilated pore domain, an outward movement of NTD, and an overall expanded structure in Model-II (*SI Appendix*, Fig. S10), highlighting that our structures are captured in a unique open conformation.

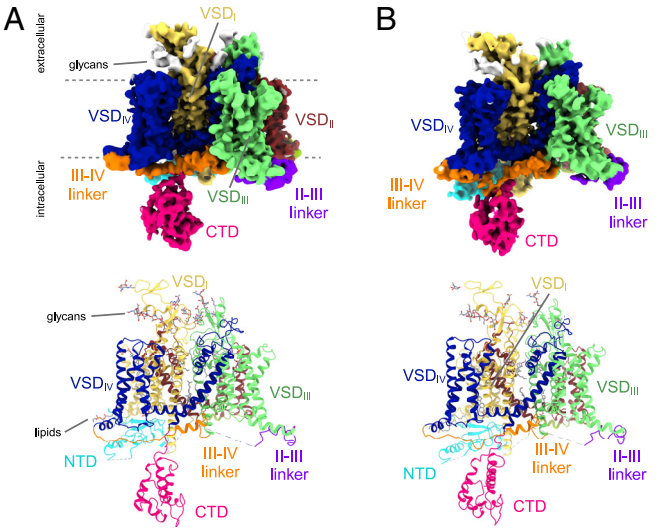

Fig. 1. Cryo-EM structures of full-length $hNa_v1.5$. (*A*) Side view of the cryo-EM reconstruction of Model-I. Individual domains and interdomain linkers are segmented and color-coded. The *Lower* panel depicts the atomic structure of Model-I including the resolved CTD, interdomain linkers, lipid molecules, and covalently attached glycans. The structural features are segmented and color-coded according to the density map. (*B*) Side view of the cryo-EM reconstruction (*Top*) and atomic structure (*Bottom*) of Model-II. Color-coded according to (*A*).

Sequential Activation of Gating Charges Is Coupled with Fast Inactivation. Capturing VSDs in different conformations is necessary to understand the precise activation and inactivation mechanisms of $Na_v1.5$. The VSDs in the previous open and inactive state structures of $Na_v1.5$ show similar conformations and upward gating charges (GCs) (*SI Appendix*, Fig. S9) (12, 15, 28). The gating charges in VSD_{II} and VSD_{IV} in $rNa_v1.5c$/QQQ (PDB ID: 7FBS) and $Na_v1.5$-E1784K (PDB ID: 7DTC) structures moved upward compared to the Model-II (Fig. 2*B* and *SI Appendix*, Fig. S11). Specifically, multiple salt bridge interactions are rearranged, and two unique p-cation interactions are established between occluding residue (OR) and R4 of Model-II (*SI Appendix*, Figs. S11 and S12). Three GCs in VSD_{II} and VSD_{IV} with minimal outward translocation are positioned above the OR, indicating a less depolarized state. In contrast, VSD_I and VSD_{III} are in fully activated conformation with three and four GCs positioned above the OR, respectively. In addition, structural morphing of Model-II (open state) to $Na_v1.5$-E1784K (intermediate inactivated state) in VSD_{IV} reveals an upward movement of gating charges while the pore diameter decreases (Movie S1). The graded movement of GCs in VSDs indicates that the voltage-dependent activation of GCs in $S4_{IV}$ is coupled to the fast inactivation process. Although our structure was not captured

at a depolarizing voltage, the altered side chain conformations compared to $Na_v1.5$-E1784K suggest a distinct activation pattern in VSDs (*SI Appendix*, Fig. S12). Previous structural and functional studies have proposed a hierarchical model of VSD activation states ($S4_{III} > S4_I > S4_{II} > S4_{IV}$) during the transition from the open state to fast inactivated state (12, 28, 29). This may explain the varying degrees of GC mobility observed across different VSDs.

Classification of our structures based on the conformational spectrum of the VSDs revealed that Model-II represents a late activated state as both $S4_{IV}$ and $S4_{II}$ adopt less activated conformations (*SI Appendix*, Fig. S12). Model-I represents early inactivated states of $hNa_v1.5$ as $S4_{IV}$ and $S4_{II}$ are in activated conformations (*SI Appendix*, Fig. S12). Comparison of our structures with that of $Na_v1.5$-E1784K (PDB ID: 7DTC; intermediate inactivated state) revealed a sequential activation of $S4_{IV}$ and $S4_{II}$ as they transition from the open state of Model-II to the intermediate inactivated state of $Na_v1.5$-E1784K (*SI Appendix*, Fig. S12).

The III-IV Linker and Interaction with the CTD. The positioning of the CTD with respect to the III-IV linker and the transmembrane core is crucial for the working mechanisms of $hNa_v1.5$. The IFM motif of Model-II is loosely docked into the hydrophobic receptor pocket formed by the $S4_{III}$-$S5_{III}$ linker and the intracellular ends of $S5_{IV}$ and $S6_{IV}$ (Fig. 2*C*, and *SI Appendix*, Fig. S13 *A* and *B*). This positioning differs from other mammalian $Na_v1.5$ structures as follows. First, the short α-helix that immediately follows the IFM motif and the IFM receptor exhibits a downward displacement (Fig. 2*C* and *SI Appendix*, Fig. S13*B*). The IFM motif is engaged in hydrophobic interactions within the receptor binding pocket (Fig. 2*D* and *SI Appendix*, Fig. S13*B*). The stability of the pocket is primarily maintained by a cluster of hydrophobic residues and polar contacts (Fig. 2 *D* and *E* and *SI Appendix*, Fig. S13 *C* and *D*). Altered side chain conformations of N1765, F1473, and Q1476 cause a downward shift in the IFM motif without fully displacing it from the receptor (Fig. 2*F* and *SI Appendix*, Fig. S13*E*). This structural rearrangement is further stabilized by the interaction between D1484 and K1492, located in the short α-helix (Fig. 2*E*). Second, a significant change in the conformation of the $S0_{IV}$ helix and the connecting loop of the III-IV linker. The N-terminal end of the $S0_{IV}$ moved ~4 to 6 Å outward which caused a significant displacement of the flexible loop of the III-IV linker (Fig. 2 *G* and *H*). As a consequence of this transition, the IFM motif is repositioned but not displaced from the receptor despite the channel being in the open state (Movie S1).

Moreover, the position of the EF-hand domain of the CTD is resolved in our cryo-EM structures. The CTD is positioned closer to the III-IV linker in Model-II compared to Model-I. The superimposition of Model-I and Model-II shows that the position of the CTD differs by ~9° (Fig. 3 *A* and *B* and Movie S2). Normal mode analysis (NMA) shows similar dynamics of the CTD in both structures and transient interactions between the CTD and the III-IV linker (Movie S3). The comparison of the CTD in our structures with that in the Na_vPaS and Na_vPas-$Na_v1.7$ chimera structures revealed significant differences in the positioning of the III-IV linker. In our structures, the EF-hand domain interacts with the flexible loop of the III-IV linker rather than being positioned on the short α-helix of the III-IV linker. In Model-II, this interaction results in the bending of the flexible loop of the III-IV linker at residues K1504 and K1505 (Fig. 3 *A* and *C*). This causes an inward movement of the $S0_{IV}$ helix and the short α-helix of the III-IV linker (Fig. 3 *A* and *C* and Movie S2). Both positively charged residues are positioned near the negatively charged surface of αI and αV helices of the EF-hand domain of the CTD (Fig. 3*C*). NMA and our structures show that the III-IV linker is within interacting distance of the CTD, highlighting the intrinsic dynamics of this region. Despite the flexibility of the CTD limiting the analysis of high-resolution details, we show that K1505 and K1504 in the III-IV linker form direct interactions with E1788 and E1867 in the CTD in Model-II, respectively (*SI Appendix*, Fig. S14). Site-directed mutagenesis coupled with electrophysiological measurements were used to assess the importance of this interface in the inactivation kinetics of $hNa_v1.5$. Our data revealed that charge reversal mutations K1504E and K1505E in the III-IV linker alter $hNa_v1.5$ inactivation parameters. Mutations K1504E and K1505E resulted in a faster time course of inactivation compared to WT (Fig. 3*D*, *SI Appendix*, Fig. S15*A* and Table S2). Alterations in the inactivation parameters were also observed when charge reversal mutations (E1788K and E1867K) were introduced into the EF-hand domain of the CTD. Additionally, all four mutants produced destabilization in inactivation as illustrated by a significant hyperpolarized shift in steady-state inactivation (Fig. 3*E* and *SI Appendix*, Table S2). We also found that one of the mutants, E1788K, displayed a slower recovery (Fig. 3*F* and *SI Appendix*, Table S2). While none of the mutants significantly affected current densities (*SI Appendix*, Fig. S15*B*), K1504E and E1867K exhibited a depolarized shift in the conductance curve (Fig. 3*E* and *SI Appendix*, Table S2), suggesting delayed activation. Our results show that the dynamics between the CTD and the III-IV linker are crucial for the transition of $hNa_v1.5$ from the open state to the inactivated state during the kinetic cycle.

Conformation of the Two-Tier Hydrophobic Activation Gate in the Open State. The opening and closing of the activation gate regulate the influx of sodium ions into the cells. In our structures, the activation gate is open. We used the position of two hydrophobic rings at the lower part of the S6 helices as a reference for the comparison of the activation gate in our two structures with the $Na_v1.5$-E1784K (PDB ID: 7DTC, intermediate inactive state) and $rNa_v1.5c$/QQQ (PDB ID: 7FBS, open state) structures (16). The residues on the top layer are L409, L935, I1466, and I1768. The bottom layer residues are A413, L938, I1470, and I1771. In the open state structure of $rNa_v1.5c$/QQQ, the average pore diameter is ~10.2 Å at the top layer and ~10.3 Å at the bottom layer (Fig. 3*G*). The average pore diameter in the upper and lower layer of $Na_v1.5$-E1784K is 8.4 Å and 8.7 Å (Fig. 3*G*) indicative of an intermediate state. Comparison with Model-I showed that average pore diameters at the top and bottom layer are ~10 Å and ~10.3 Å and closely resemble those of $rNa_v1.5c$/QQQ (Fig. 3 *G–I*) (15). We observed an even larger activation gate diameter in Model-II, measuring ~11 Å each at the top and bottom layers (Fig. 3 *G–I*). Thus, we propose that Models I and II represent different open state conformations of the activation gate. Notably, we observed a synchronized movement of the S6 helices from the pore axis, leading to an equivalent pore diameter of the activation gate in both structures (Movie S1). The asymmetric movements of S6 helices in the $rNa_v1.5c$/QQQ structure are caused by a distorted conformation of the IFM receptor because of the presence of the QQQ mutation. Therefore, it is plausible that $rNa_v1.5c$/QQQ may not accurately depict the open state conformation of the activation gate. In summary, our structures demonstrate the open state of activation gates, highlighting a previously unseen positioning of the IFM motif.

MD Analysis of Na^+ Conductance in the Open Activation Gate. To investigate the Na^+ conductance of our open state structure, we conducted MD simulations of Model-II. Restraining the Cα positions with harmonic potentials prevented the pore from

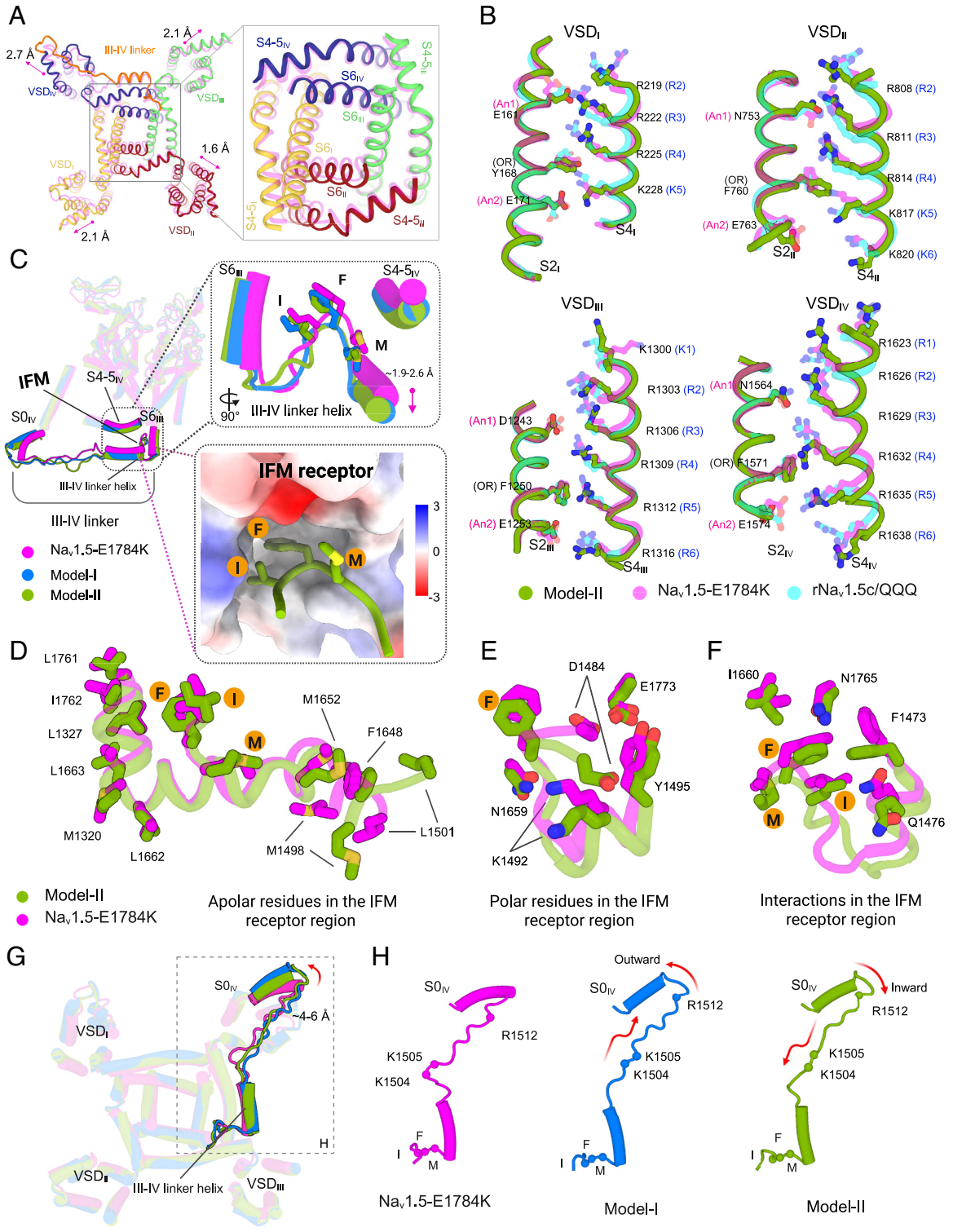

Fig. 2. Insights into key functional regions of hNa$_v$1.5. (*A*) The intracellular view of the structural superimposition of Model-II (bold color) and Na$_v$1.5-E1784K (PDB ID: 7DTC, transparent magenta) displays a lateral dilation of the VSDs. The inset shows the dilation of the PD. (*B*) Comparative analysis of the conformation of GC residues of individual VSDs in Model-II, Na$_v$1.5-E1784K (PDB ID: 7DTC, magenta), and rNa$_v$1.5c/QQQ (PDB ID: 7FBS, cyan). GC residues are shown in stick representation. An1 and An2 denote anion1 and anion2, respectively. OR denotes the occluding residue. For clarity, only the S2 and S4 segments of all the VSDs are shown. (*C*) Superimposition of Model-I (blue), Model-II (green), and Na$_v$1.5-E1784K (magenta). The III-IV linker and its connecting S0$_{IV}$ helix are highlighted and labeled. The conformational changes of the IFM and III-IV linker helix are shown in the upper right inset. The lower inset shows the electrostatic surface potential of the IFM receptor bound to the IFM motif of Model-II. The IFM residues in the receptor are highlighted. (*D*) Overall structural alignment between Model-II (green) and Na$_v$1.5-E1784K (magenta). Conserved residues involved in hydrophobic interactions at the IFM receptor of Model-II (green) and Na$_v$1.5-E1784K (magenta) are shown in bold stick. The IFM residues in the receptor are highlighted. (*E*) Conserved residues involved in polar interactions at the IFM receptor after overall structural alignment. D1484 moves downward from Na$_v$1.5-E1784K (magenta) to Model-II (green). D1484 and K1492 form a salt bridge in Model-II. The IFM residues in the receptor are highlighted. (*F*) Interaction between the IFM motif and the receptor pocket residues after structural alignment. The side chain of F1473 has moved downward which causes displacement of the IFM motif. Key residues are shown in stick representation. The IFM residues in the receptor are highlighted. (*G*) The III-IV linker and outward tilting of the S0$_{IV}$ helix are highlighted in the overlay of Model-I, Model-II, and Na$_v$1.5-E1784K. (*H*) The translation of the flexible loop of the III-IV linker is associated with the tilting of the S0$_{IV}$ helix. The Cα sphere represents the positions of three mutational hotspot residues.

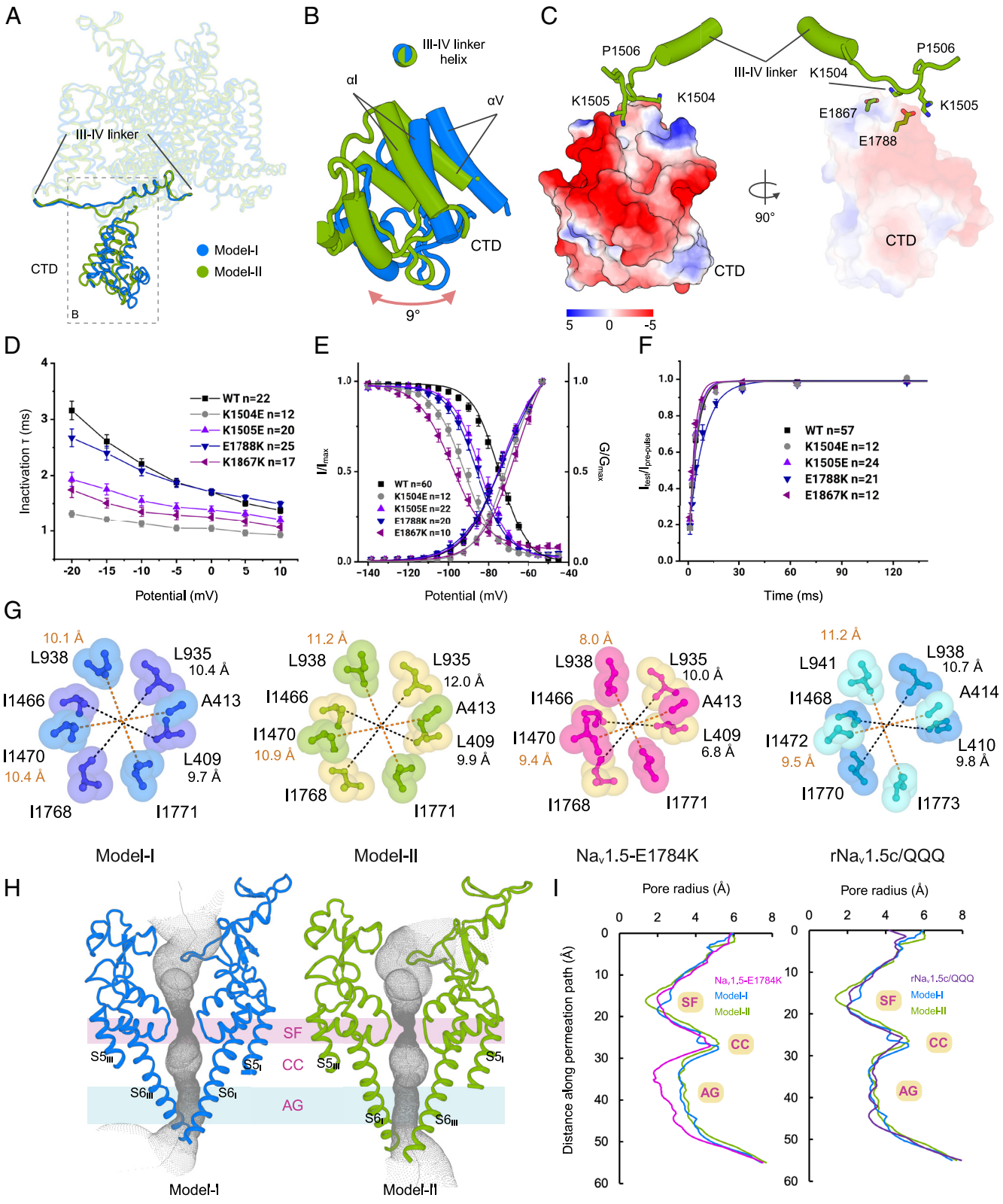

Fig. 3. Conformational dynamics of the CTD, kinetic analysis, and the comparison of the activation gate in the open state. (*A*) Superimposition of Model-I (blue) and Model-II (green). The positions of the III-IV linker and CTD are highlighted. (*B*) The position of the CTD differs by > 9° between Model-I and Model-II. (*C*) Key residues K1504 and K1505 of the III-IV linker are near the negatively charged surface of the CTD (*Left*). K1504 of the III-IV linker interacts with E1867 in the CTD. K1505 of the III-IV linker interacts with E1788 in the CTD of Model-II (*Right*). (*D*) Electrophysiological recordings of current–voltage relationships displayed a faster time course of inactivation for K1504E, K1505E, and E1867K. (*E*) Charge-reversal mutants K1504E, K1505E, E1788K, and E1867K cause a hyperpolarized shift in steady-state inactivation. A depolarized shift in the conductance curve was seen for K1504E and E1867K. (*F*) E1867K displayed a slower recovery from inactivation. (*G*) Comparison of the activation gate diameter in Model-I, Model-II, $Na_v1.5$-E1784K (PDB ID: 7DTC), and $rNa_v1.5c$/QQQ (PDB ID: 7FBS). The black and orange dashed lines represent the diameter at the *Top* and *Bottom* layers of the activation gate, respectively. (*H*) The permeation paths of Model-I and Model-II are shown as gray dots. SF: selectivity filter, CC: central cavity, AG: activation gate. (*I*) The corresponding pore radii are compared with that of $Na_v1.5$-E1784K and $rNa_v1.5c$/QQQ.

collapsing to a dehydrated and nonconducting conformation while allowing for the reorganization of side chains. At the transmembrane voltage (TMV) of 0 mV, the channel exhibits a nonconducting state due to a substantial reduction in hydration within the vicinity of the activation gate. This localized dehydration is a consequence of the hydrophobic residues that line the gate, resulting in a lower water density compared to the surrounding bulk solvent (Fig. 4 *A* and *B*). Conversely, at voltages > + 350 mV and < − 350 mV, we observed an increase in pore hydration at the activation gate (Fig. 4*A*). The pore remains hydrated and conductive at TMV above +350 mV and below −350 mV (Fig. 4*A*). At lower TMV (~100 mV), the water density at the activation gate is significantly less than that of the bulk solvent, resulting in a partly hydrated pore (Fig. 4*A*). This suggests high free energy barriers for sodium ions permeation through the channel. Sodium ion conduction was quantified by monitoring the cumulative number of sodium ion permeation events through the channel during the 600 ns long MD trajectories. Half permeation events in either direction were not counted to ensure that both the selectivity filter and the activation gate were fully

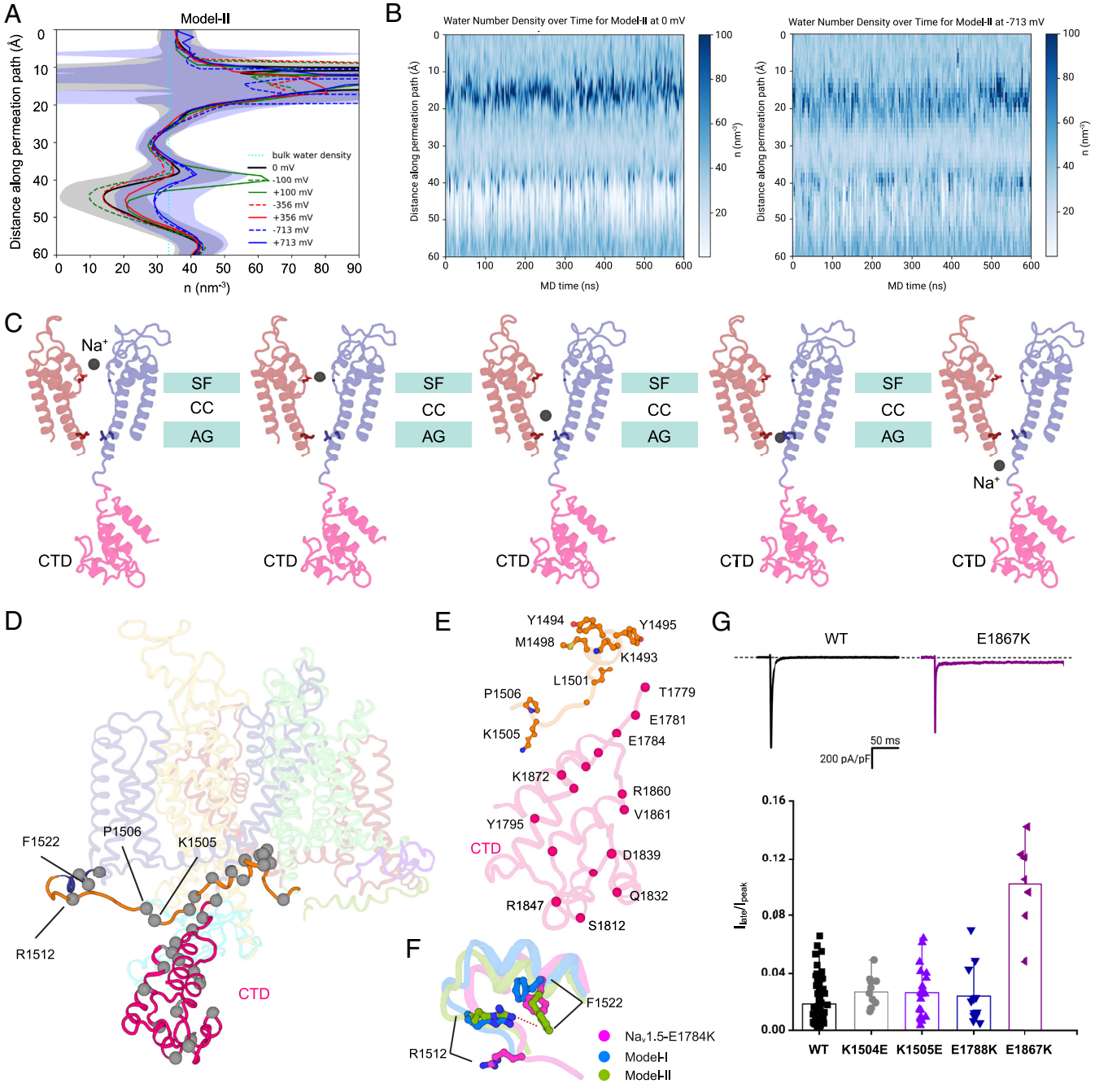

Fig. 4. MD analysis of Model-II and structural mapping of mutations linked to BrS and LQT3. (*A*) Average hydration along the pore axis at different TMV. At lower TMV (~100 mV), the AG region is dehydrated. At higher TMV (>350 mV), pore hydration is increased (dashed, solid blue, and red curve) at the AG. The dotted cyan line indicates bulk water density. Solid and dashed curves represent hydration profiles at positive and negative TMV, respectively. (*B*) Hydration profile along the pore axis at 0 mV and −713 mV TMV for Model-II during the 600 ns MD simulation. (*C*) Snapshots of a Na^+ (black sphere) permeation event during MD simulation. SF: selectivity filter, CC: central cavity, AG: activation gate. (*D*) Structural mapping of mutation hotspot residues (sphere). (*E*) A cluster of selected mutations associated with BrS and LQT3 in the region of the III-IV linker and CTD. (*F*) Interaction between R1512 and F1522 in Model-I (blue), Model-II (green), and $Na_v1.5$-E1784K (magenta). The π-cation interaction occurs exclusively in Model-II. (*G*) E1867K mutation presented a significant increase in persistent current, but no change in persistent current was observed in K1504E, K1505E, and E1788K.

conductive while recording conductance events. During the 600 ns simulation, we observed three spontaneous Na^+ permeation events (Fig. 4*C*, *SI Appendix*, Table S3, and Movie S4) as well as increased hydration at the activation gate region (solvent density: 19.919 molecules/nm^3). We further calculated the time-averaged pore radius profiles at varying TMV to locate the channel residues that respond to the application of TMV and lead to increased hydration at the activation gate (Fig. S16 *A* and *B*). Our analysis shows that the residues at the selectivity filter and the activation gate respond the most to the applied TMV, thereby increasing the possibility of sodium ion permeation through the channel.

Distributions of Disease-Causing Mutations in the NTD and CTD. Previous hNa$_v$1.5 structures have not resolved intracellular regions that contain the majority of hNa$_v$1.5 disease-causing mutations. Our cryo-EM structures include the previously unresolved NTD and the CTD of hNa$_v$1.5. This allowed us to systematically map the disease-causing mutations linked to LQT3 and BrS in these regions. Analysis of mutations in the NTD and its interacting $S6_I$ helix, as well as in the CTD and its interacting III-IV linker, showed a distinct pattern of distribution in the structures (Fig. 4*D* and *SI Appendix*, Fig. S17). We found that mutations associated with LQT3 and BrS are dispersed evenly in the NTD (*SI Appendix*, Fig. S17) while a cluster of mutations is present in the III-IV linker and the adjacent region of the CTD (Fig. 4 *D* and *E*). Mutations in the bending region of the III-IV linker, specifically at K1505 and P1506 of the KPQ sequence, can lead to LQT3 and BrS (Fig. 4*E*) (29–33). P1506 is crucial in shaping the curvature of the III-IV linker, which enables the interaction between K1504-K1505 and the CTD (Movie S2). Our structures further revealed an important mutational hotspot at the C-terminal end of the III-IV linker and its connecting $S0_{IV}$ helix where residue R1512 engages in a π-cation interaction with F1522 in Model-II (Fig. 4*F* and Movies S1 and S2). This interaction is disrupted in Na$_v$1.5-E1784K, suggesting that the π-cation interaction is transient and reliant on the conformation of the $S0_{IV}$ helix. Mutation R1512W can lead to a robust π-stacking interaction with F1522 that limits the flexibility of the $S0_{IV}$ helix and its connecting III-IV linker and leads to the reported changes in hNa$_v$1.5 kinetics in BrS (34, 35). It is well established that mutations leading to LQT3, found in regions associated with inactivation, often present with an increase in persistent current. Here, we observed that the introduction of mutant E1867K resulted in a significant increase in late current (Fig. 4*G*), further supporting the contribution of this region to cardiac channelopathies.

Discussion

Our cryo-EM studies revealed structural features of hNa$_v$1.5 and highlighted the conformational dynamics around the VSDs and CTD as critical for sodium channel function. Our native, untruncated structures of hNa$_v$1.5 are captured in the open state. Importantly, the IFM motif is repositioned within its receptor but not displaced, providing crucial insights into the fast inactivation mechanism. The consequence of this repositioning of the IFM and the III-IV linker is transduced allosterically to the S6 segments to facilitate the opening of the activation gate. These potential allosteric conformational changes may be attributed to the overall increased lateral dilation of our structure. Together, we demonstrated how the expansion of the activation gate and pore domain are interconnected, along with the overall expansion of the entire structure through concerted movements of the pore-forming segments.

Gating in voltage-dependent ion channels is regulated through voltage-sensing domains (VSDs), which detect voltage differences across the membrane, change conformation, and exert force on the pore to open or close it. Previously, bacterial and eukaryotic voltage-gated ion channel structures were captured in the expanded pore or open conformation by introducing truncations, mutations, and/or using blockers (15, 36, 37). The rat Na$_v$1.5c/QQQ structure (PDB ID: 7FBS) is one such structure that was captured in a pore-expanded conformation using mutations in the IFM region and a pore blocker (15). Our full-length hNa$_v$1.5 structures were captured in the pore-expanded conformation with unique inactivation gate positioning (Fig. 2 *C* and *D*), CTD (Fig. 3 *A* and *B*), and the III-IV linker interactions (Fig. 3*C*), and conformations in GCs (*SI Appendix*, Figs. S7 and S8). In addition, a structural comparison of previous Na$_v$1.5 structures with Model-II showed a different extent of overall dilations (*SI Appendix*, Fig. S18). We speculate that using full-length protein allowed us to capture the open state, with the intact loops and intracellular domains likely playing a key role in stabilizing this conformation. Additionally, producing the protein in the GnTi- expression system may have resulted in different glycosylation patterns in the extracellular region that may have stabilized this state. Another possibility is that the presence of uncharacterized lipid molecules may have contributed to stabilizing the pore domain in the open conformation.

Our structural analysis elucidates the interaction between the III-IV linker and the CTD in full-length Na$_v$1.5. Specifically, our findings demonstrate that residues K1504 and K1505 in the III-IV linker interact with residues E1867 and E1788 in the CTD. This contrasts with a prior study that, using a III-IV linker peptide and an isolated CTD, reported interactions involving residues K1504 and K1505 with L1786, S1787, D1790, Y1795, and C1850 of the CTD (38). The sequence alignment of all the human Na$_v$ subtypes (1.1 to 1.9) shows that the residues at the III-IV linker are highly conserved across the Na$_v$ channel family. The residues involved in the interaction with the CTD are also conserved except for an E1699 to G1699 substitution in hNa$_v$1.9. Thus, our structure uncovers a distinct interaction interface between the III-IV linker and the CTD, that allosterically regulates VSDs and pore opening of the channel. The high conservation of these residues across Na$_v$ channels suggests a common mechanism for fast inactivation. This underlines the importance of studying Na$_v$1.5 and other Na$_v$ family proteins in the context of a full-length protein.

Our structures further reveal unexpected and unique open states that shed light on the mechanism by which hNa$_v$1.5 transitions from an open to an inactivated state (Fig. 5). These structures further enabled us to identify several key residues related to LQT3 and BrS in the NTD, the III-IV linker, and the CTD. Notably, our study reveals the electromechanical coupling mechanisms among VSDs, the III-IV linker, and the S5–S6 segments, and their previously unanticipated relationship with the CTD. In conclusion, our findings reveal structural insights into the molecular mechanism of fast inactivation and provide an essential roadmap for studying the regulation of the channel by its numerous protein partners, which interact predominantly with the intracellular regions of Na$_v$1.5.

Materials and Methods

Cloning of the Full-Length Human Na$_v$1.5 Expression Vector. Codon-optimized full-length human Na$_v$1.5 (hNa$_v$1.5) cDNA was synthesized (GenScript, NJ) and cloned into a modified pCDNA3.1 vector containing a twin-Strep tag and a TEV site at the N-terminus and an HRV 3C site and a FLAG tag at the C-terminus of the channel cDNA. Mutations K1504E, K1505E, E1788K, and E1867K were introduced in the Na$_v$1.5 cDNA via site-directed mutagenesis (Quick change II mutagenesis kit, Agilent, CA). All plasmids generated were verified by Sanger sequencing.

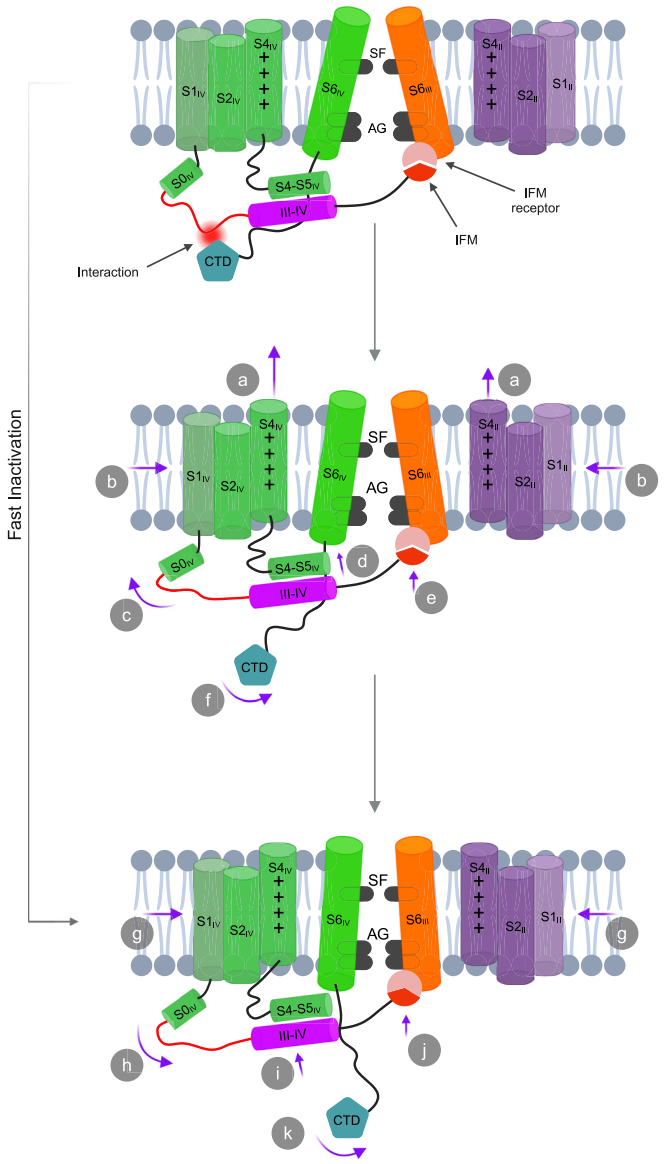

Fig. 5. Mechanism of fast inactivation. Transition from the open state to the inactivated state. The conformational changes in each state are assigned with letters. (*a*) $S2_{II}$ and $S4_{IV}$ sequentially move upward, transitioning from a partially depolarized to a fully depolarized conformation. (*b*) Overall dilation is reduced. (*c*) Then the $S0_{IV}$ helix is slanted outward and forms an extended conformation of the flexible loop of the III–IV linker. (*d*) S4–$S5_{IV}$ linker and III-IV linker helices move upward. (*e*) IFM motif undergoes a transition from a loosely bound state to a semitight conformation. (*f*) The CTD partially moves away from the III-IV linker, resulting in a loss of electrostatic interactions. Transition from the intermediate state to inactivated state: (*g*) A further reduction in overall dilation. (*h*) $S0_{IV}$ is slanted inward and forms a relaxed conformation of the flexible loop of the III-IV linker. (*i*) S4–$S5_{IV}$ linker and III-IV linker helices move further upward. (*j*) IFM motif undergoes a shift from a semitight conformation to a tightly bound state. (*k*) The CTD moves further away and retains a dynamic conformation. Schematics are not drawn to scale.

Expression of $hNa_v1.5$. Full-length human $Na_v1.5$ was recombinantly produced in Expi293F GnTI- suspension cells (ThermoFisher). Cells were grown in Expi293 expression medium (ThermoFisher) at 37 °C in 8% CO2. Transient transfections of pCDNA3.1-$hNa_v1.5$ were done with ExpiFectamine 293 (ThermoFisher). Cells were harvested ~48 h post transfection, and the cell pellets were flash-frozen in liquid nitrogen.

Purification of the Full-Length Human Cardiac Sodium Channel. Pellets from 6 L of cells were used for the purification of $hNa_v1.5$. The cell pellet was first washed with 1X PBS and subsequently suspended in lysis buffer containing 25 mM HEPES (pH 7.4), 150 mM NaCl, 0.1 mM EGTA, and 10% glycerol (buffer A). A protease inhibitor cocktail was added to the suspension before homogenization. The membrane fraction was collected through ultracentrifugation, then resuspended and dissolved in buffer A supplemented with protease inhibitors, 1% (w/v) n-dodecyl-β-D maltopyranoside (DDM, Anatrace), and 0.1% (w/v) cholesteryl hemisuccinate (CHS, Anatrace). The suspension was gently stirred at 4 °C for 2 h. The cell lysate was subjected to ultracentrifugation (30,000 RPM, 4° C, 30 min). The supernatant was incubated for 2 h with 5 mL of anti-Flag M2 affinity gel that had been equilibrated in advance with buffer B (buffer A supplemented with 0.06% (w/v) glycol-diosgenin (GDN, Anatrace) and protease inhibitor cocktail). The protein-bound FLAG M2 affinity gel was washed with 10-column volumes (CV) of buffer B. The bound protein was eluted using buffer B supplemented with 200 μg/mL of FLAG peptide. The eluent was incubated for 1.5 h with 3 mL of Strep-Tactin XT 4Flow (IBA) high-capacity resin that had been pre-equilibrated with buffer B. The resin was rinsed with 5 CVs of buffer B, followed by elution of the protein using buffer B containing 50 mM biotin (IBA). The eluted protein was concentrated using a 100-kDa cut-off concentrator (Millipore) and subsequently purified using a Superose 6 increase 10/300 gL column (Cytiva) in buffer C (25 mM HEPES at pH 7.4, 150 mM NaCl, 0.1 mM EGTA, and 0.06% GDN). The peak fractions of the purified protein were pooled and concentrated to approximately 8 μM for cryo-EM analysis.

Detailed materials and methods consisting of cell culture, whole-cell electrophysiology, cryo-EM sample preparation, cryo-EM data collection, image processing and 3D reconstruction, and MD simulations are described in *SI Appendix, Materials and Methods*.

Data, Materials, and Software Availability. The cryo-EM structures are deposited in the Protein Data Bank (PDB) and Electron Microscopy Data Bank (EMDB) under the following accession numbers: Model-I: PDB ID: 8VYJ (39), EMDB ID: EMD-43662 (40); Model-II: PDB ID: 8VYK (41), EMDB ID: EMD-43663 (42). The raw cryo-EM movies corresponding to this study are deposited in the Electron Microscopy Public Image Archive (EMPIAR) under the Accession No: EMPIAR-12514 (43). All other data supporting the findings of this study are available in the manuscript and its supporting information. Reasonable requests for resources and reagents should be directed to and will be fulfilled by the Lead Contact, Krishna Chinthalapudi (chinthalapudi.1@osu.edu). All unique reagents generated in this study are available from the Lead Contact with a completed Materials Transfer Agreement.

ACKNOWLEDGMENTS. Electron microscopy data were acquired at the Center for Electron Microscopy and Analysis at The Ohio State University. We thank the Ohio Supercomputer Center for high-performance computing resources.This work was supported by National Institutes of Health grant R01HL094450 (I.D.) and the Frick Center for Heart Failure via a Synergy Award from the Dorothy M. Davis Heart and Lung Research Institute at The Ohio State University Wexner Medical Center (I.D.) and start-up funds from The Ohio State University College of Medicine (S.M.H., I.D., and K.C.).

Author affiliations: [a]Department of Physiology and Cell Biology, Dorothy M. Davis Heart and Lung Research Institute, College of Medicine, The Ohio State University, Columbus, OH 43210; [b]Frick Center for Heart Failure and Arrhythmia Research, The Ohio State University Wexner Medical Center, Columbus, OH 43210; [c]Division of Medicinal Chemistry and Pharmacognosy, College of Pharmacy, The Ohio State University, Columbus, OH 43210; [d]Center for Electron Microscopy and Analysis, College of Engineering, The Ohio State University, Columbus, OH 43210; and [e]Translational Data Analytics Institute at The Ohio State University, Columbus, OH 43210

1. A. L. Hodgkin, A. F. Huxley, A quantitative description of membrane current and its application to conduction and excitation in nerve. *J. Physiol.* **117**, 500–544 (1952).
2. C. A. Remme, A. A. Wilde, Targeting sodium channels in cardiac arrhythmia. *Curr. Opin. Pharmacol.* **15**, 53–60 (2014).
3. C. Antzelevitch *et al.*, The role of late I Na in development of cardiac arrhythmias. *Handb. Exp. Pharmacol.* **221**, 137–168 (2014).
4. C. A. Remme, SCN5A channelopathy: Arrhythmia, cardiomyopathy, epilepsy and beyond. *Philos. Trans. R Soc. Lond B Biol. Sci.* **378**, 20220164 (2023).
5. W. A. Catterall, The molecular basis of neuronal excitability. *Science* **223**, 653–661 (1984).
6. M. Noda *et al.*, Primary structure of Electrophorus electricus sodium channel deduced from cDNA sequence. *Nature* **312**, 121–127 (1984).
7. Y. Jiang *et al.*, X-ray structure of a voltage-dependent K+ channel. *Nature* **423**, 33–41 (2003).

8. D. Noble, The surprising heart: A review of recent progress in cardiac electrophysiology. *J. Physiol.* **353**, 1–50 (1984).
9. J. W. West *et al.*, A cluster of hydrophobic amino acid residues required for fast Na(+)-channel inactivation. *Proc. Natl. Acad. Sci. U.S.A.* **89**, 10910–10914 (1992).
10. X. Pan *et al.*, Structure of the human voltage-gated sodium channel Na(v)1.4 in complex with beta1. *Science* **362**, eaau2486 (2018).
11. Z. Li *et al.*, Structure of human Na(v)1.5 reveals the fast inactivation-related segments as a mutational hotspot for the long QT syndrome. *Proc. Natl. Acad. Sci. U.S.A.* **118**, e2100069118 (2021).
12. D. Jiang *et al.*, Structure of the cardiac sodium channel. *Cell* **180**, 122–134.e110 (2020).
13. H. Shen, D. Liu, K. Wu, J. Lei, N. Yan, Structures of human Na(v)1.7 channel in complex with auxiliary subunits and animal toxins. *Science* **363**, 1303–1308 (2019).
14. Z. Yan *et al.*, Structure of the Na(v)1.4-beta1 complex from electric Eel. *Cell* **170**, 470–482.e411 (2017).
15. D. Jiang *et al.*, Open-state structure and pore gating mechanism of the cardiac sodium channel. *Cell* **184**, 5151–5162.e5111 (2021).
16. Y. Liu, C. A. Z. Bassetto Jr., B. I. Pinto, F. Bezanilla, A mechanistic reinterpretation of fast inactivation in voltage-gated Na(+) channels *Nat. Commun.* **14**, 5072 (2023).
17. H. Shen *et al.*, Structure of a eukaryotic voltage-gated sodium channel at near-atomic resolution. *Science* **355**, eaal4326 (2017).
18. I. Deschenes, L. Chen, R. G. Kallen, M. Chahine, Electrophysiological study of chimeric sodium channels from heart and skeletal muscle. *J. Membr Biol.* **164**, 25–34 (1998).
19. I. Deschenes, E. Trottier, M. Chahine, Implication of the C-terminal region of the alpha-subunit of voltage-gated sodium channels in fast inactivation. *J. Membr Biol.* **183**, 103–114 (2001).
20. P. B. Bennett, K. Yazawa, N. Makita, A. L. George Jr., Molecular mechanism for an inherited cardiac arrhythmia. *Nature* **376**, 683–685 (1995).
21. H. K. Motoike *et al.*, The Na+ channel inactivation gate is a molecular complex: A novel role of the COOH-terminal domain. *J. Gen Physiol.* **123**, 155–165 (2004).
22. M. Mantegazza, F. H. Yu, W. A. Catterall, T. Scheuer, Role of the C-terminal domain in inactivation of brain and cardiac sodium channels. *Proc. Natl. Acad. Sci. U.S.A.* **98**, 15348–15353 (2001).
23. J. D. Kapplinger *et al.*, Enhanced classification of brugada syndrome-associated and long-QT syndrome-associated genetic variants in the SCN5A-encoded Na(v)1.5 cardiac sodium channel. *Circ. Cardiovasc. Genet.* **8**, 582–595 (2015).
24. X. Pan *et al.*, Molecular basis for pore blockade of human Na(+) channel Na(v)1.2 by the mu-conotoxin KIIIA. *Science* **363**, 1309–1313 (2019).
25. X. Fan, J. Huang, X. Jin, N. Yan, Cryo-EM structure of human voltage-gated sodium channel Na(v)1.6. *Proc. Natl. Acad. Sci. U.S.A.* **120**, e2220578120 (2023).
26. X. Huang *et al.*, Structural basis for high-voltage activation and subtype-specific inhibition of human Na(v)1.8. *Proc. Natl. Acad. Sci. U.S.A.* **119**, e2208211119 (2022).
27. L. Tonggu *et al.*, Dual receptor-sites reveal the structural basis for hyperactivation of sodium channels by poison-dart toxin batrachotoxin. *Nat. Commun.* **15**, 2306 (2024).
28. Z. Li *et al.*, Structural basis for pore blockade of the human cardiac sodium channel Na(v) 1.5 by the antiarrhythmic drug quinidine*. *Angew. Chem. Int Ed. Engl.* **60**, 11474–11480 (2021).
29. D. Nuyens *et al.*, Abrupt rate accelerations or premature beats cause life-threatening arrhythmias in mice with long-QT3 syndrome. *Nat. Med.* **7**, 1021–1027 (2001).
30. R. Chandra, C. F. Starmer, A. O. Grant, Multiple effects of KPQ deletion mutation on gating of human cardiac Na+ channels expressed in mammalian cells *Am. J. Physiol.* **274**, H1643–H1654 (1998).
31. Q. Wang *et al.*, SCN5A mutations associated with an inherited cardiac arrhythmia, long QT syndrome. *Cell* **80**, 805–811 (1995).
32. J. D. Kapplinger *et al.*, Spectrum and prevalence of mutations from the first 2,500 consecutive unrelated patients referred for the FAMILION long QT syndrome genetic test. *Heart Rhythm* **6**, 1297–1303 (2009).
33. S. Saber *et al.*, Complex genetic background in a large family with Brugada syndrome. *Physiol Rep* **3**, e12256 (2015).
34. I. Deschenes *et al.*, Electrophysiological characterization of SCN5A mutations causing long QT (E1784K) and Brugada (R1512W and R1432G) syndromes. *Cardiovasc. Res.* **46**, 55–65 (2000).
35. M. B. Rook *et al.*, Human SCN5A gene mutations alter cardiac sodium channel kinetics and are associated with the Brugada syndrome. *Cardiovasc Res.* **44**, 507–517 (1999).
36. V. Burtscher *et al.*, Structural basis for hyperpolarization-dependent opening of human HCN1 channel. *Nat. Commun.* **15**, 5216 (2024).
37. M. J. Lenaeus *et al.*, Structures of closed and open states of a voltage-gated sodium channel. *Proc. Natl. Acad. Sci. U.S.A.* **114**, E3051–E3060 (2017).
38. B. R. Gardill *et al.*, The voltage-gated sodium channel EF-hands form an interaction with the III-IV linker that is disturbed by disease-causing mutations. *Sci. Rep.* **8**, 4483 (2018).
39. R. Biswas, K. Chinthalapudi, Structure of full-length human cardiac sodium channel - Class I. Worldwide Protein Data Bank. https://doi.org/10.2210/pdb8vyj/pdb. Deposited 8 February 2024.
40. R. Biswas, K. Chinthalapudi, Structure of full-length human cardiac sodium channel - Class I. Electron Microscopy Data Bank. https://www.ebi.ac.uk/emdb/EMD-43662. Deposited 8 February 2024.
41. R. Biswas, K. Chinthalapudi, Structure of full-length human cardiac sodium channel - Class II. Worldwide Protein Data Bank. https://doi.org/10.2210/pdb8VYK/pdb. Deposited 8 February 2024.
42. R. Biswas, K. Chinthalapudi, Structure of full-length human cardiac sodium channel - Class II. Electron Microscopy Data Bank. https://www.ebi.ac.uk/emdb/EMD-43663. Deposited 8 February 2024.
43. R. Biswas, K. Chinthalapudi, Cryo-EM movies of human cardiac sodium channel. Electron Microscopy Public Image Archive. https://www.ebi.ac.uk/empiar/EMPIAR-12514/. Deposited 6 January 2025.